Study on Anti-icing Heat Load Distribution for a Three-Dimensional Propeller

WU Zhulong[1], *YI Xian*[2], *XIONG Huajie*[1], *ZHOU Zhihong*[1*], *TIAN Xiaobao*[1]

1. College of Architecture and Environment, Sichuan University, Chengdu 610065, P. R. China;
2. Key Laboratory of Icing and Anti/De-icing of China Aerodynamics Research and Development Center, Mianyang 621000, P. R. China

(Received 8 March 2023; revised 28 June 2023; accepted 12 October 2023)

Abstract: At present, research on the anti-icing heat loads of propeller aircraft is inadequate, while predicting the distribution of anti-icing heat loads is crucial for designing propeller aircraft anti-icing systems. A three-dimensional propeller is simulated based on the multiple reference frame and Messinger thermodynamic model to analyze the effect of the anti-icing heat load. The results indicate that the majority of the anti-icing heat loads concentrates at the leading edge of the blade, with an initial increase and subsequent decrease along the spreading direction. As the incoming flow speed increases, both the value and range of anti-icing power initially increase and then decrease. The influence of the angle of attack is negligible due to the rotating effect. The anti-icing power increases linearly as the temperature drops. Considering the provisions in Appendix C of CCAR-25, when the rotation speed is 660 r/min, the chordwise upward limit is 12.1%, the chordwise downward limit is 6.7%, and the maximum anti-icing power density is 9.5 kW/m^2. The anti-icing power of the single propeller exceeds 1.96 kW. This study provides a scientific explanation for the surface anti-icing of propeller aircraft and a theoretical basis for the installation of anti-icing systems on propeller aircraft.

Key words: aircraft deicing; anti-icing heat load; energy; rotating machine; propeller

CLC number: V211.3 **Document code:** A **Article ID:** 1005-1120(2023)06-0688-15

0 Introduction

The icing on the leading edge of an airfoil can alter the geometry of the blade[1-3], leading to a deterioration of aerodynamic performance[4] and even flight accidents. Therefore, the installation of an anti-icing system on aircraft is crucial. Currently, anti-icing systems installed in aircraft are mainly hot-air-based[5-8] or electro-thermal[9-12] anti-icing systems, which require the reasonable installation of heat source devices. Consequently, accurately predicting the distribution of heat load on the aircraft surface can facilitate the design of a more efficient anti-icing system.

Some recent studies have focused on aircraft anti-icing heat loads. Bu et al.[13] utilized the FLUENT UDF secondary development function to calculate and analyze the distribution of anti-icing heat loads on a 3D fixed-wing surface. Feng et al.[14] examined the distribution of anti-icing heat loads in an aero-engine inlet. Zhao et al.[15] analyzed the distribution of anti-icing heat loads on the surface of the horizontal tail of aircraft. Villalpando et al.[16] investigated the distribution pattern of anti-icing heat loads along the leading and trailing edges of the cross-section of wind turbines along the span based on MATLAB. Chang et al.[17] studied the anti-icing heat loads of fixed-wing aircraft by analyzing the surface anti-icing temperature distribution in the icing limit state. Bu et al.[18] developed the proper orthogonal decomposition (POD) method, a new approach for efficiently and rapidly predicting anti-icing heat

*Corresponding author, E-mail address: zhouzhihong@scu.edu.cn.

How to cite this article: WU Zhulong, YI Xian, XIONG Huajie, et al. Study on anti-icing heat load distribution for a three-dimensional propeller[J]. Transactions of Nanjing University of Aeronautics and Astronautics, 2023, 40(6): 688-702.
http://dx.doi.org/10.16356/j.1005-1120.2023.06.006

loads in 2D viscous flows with three variables. Wang[19] investigated the dynamic effects of supercooled large water droplets on the anti-icing heat load of aircraft wings. Hann et al.[20] evaluated the electro-thermal anti-icing system of two fixed-wing UAVs and observed a strong linear correlation between anti-icing load and temperature. Reid et al.[21] simulated the electro-thermal anti-icing systems of wind turbine blades on the geometric model of NREL Phase Ⅵ rotor geometry, finding that the anti-icing heat load increased initially and then decreased along the spreading direction, with the anti-icing area expanding with span. Yassin et al.[22] evaluated the distribution of anti-icing power on the surface of the NREL 5 MV wind turbine, revealing that most of the heating power was concentrated on the leading edge, lower surface, and middle blade. Hann et al.[23] investigated the required heat for an electro-thermal anti-icing system on a wind turbine and determined that the influence of wind speed and meteorological parameters was negligible. Battisti et al.[24] evaluated the impact of wind turbine size and type on the anti-icing power of wind turbines, demonstrating that the anti-icing power increases nearly proportionally to the number of blades with an increase in wind turbine blade size.

Previous research on the anti-icing heat load has primarily focused on 2D cross-sections of aircraft wings, wind turbine blades, and 3D fixed wings. However, there is currently a lack of studies on the anti-icing heat load of 3D propellers. In practice, the design of propeller anti-icing systems in engineering often relies on information from different blade sections or past experience, which lacks accuracy. Therefore, in this study, we conducted a predictive analysis on the anti-icing heat load of a 3D propeller, considering the rotational effect. Our objective was to determine the range and distribution of the anti-icing heat load on the propeller surface. This study can serve as a reference for the layout of the propeller anti-icing area and system design in engineering, leading to improved accuracy in power control of anti-icing systems.

1 Methodology

The specific thermodynamic effects and mass transfer are shown in Fig.1. In addition, during the surface ice accumulation process, it is necessary to consider the mass transfer phenomena, such as the mass of water droplets in the air impacting on the surface and the overflow of unfrozen water from the surface to nearby units. Based on the Messinger icing heat transfer model[25], the energy balance equation for the surface element is

$$\dot{Q}_{so}+\dot{Q}_{va}+\dot{Q}_{ou}+\dot{Q}_{c}+\dot{Q}_{k}=\dot{Q}_{f}+\dot{Q}_{in}+\dot{Q}_{im} \quad (1)$$

where $\dot{Q}_{so}$ is the energy of freezing water; $\dot{Q}_{va}$ the energy of water evaporation (or sublimation); $\dot{Q}_{ou}$ the energy carried by the water flowing into the current unit from the adjacent unit; $\dot{Q}_{in}$ the energy carried by the water flowing out of the current unit; $\dot{Q}_{im}$ the energy of the supercooled water droplets hitting the current unit from the air; $\dot{Q}_{f}$ the pneumatic heating of the surface owing to airflow friction; $\dot{Q}_{c}$ the convective heat transfer between the airflow and surface, and $\dot{Q}_{k}$ the energy of heat transfer between ice and water (or ice and surface).

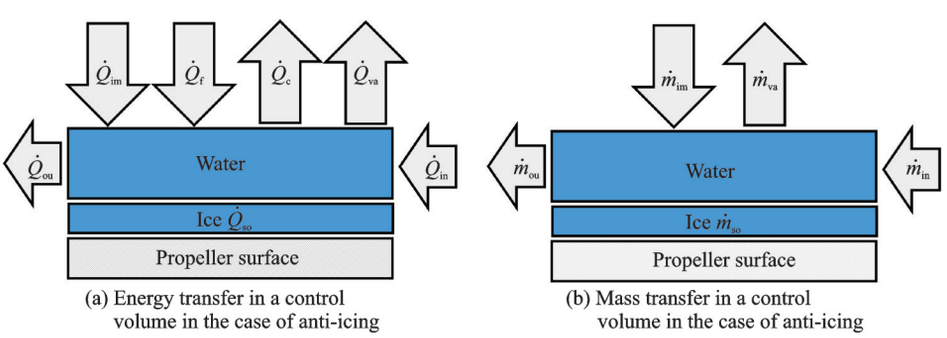

Fig.1 Diagram of energy and mass transfer model in cell during icing process

Based on the principle of mass conservation, the mass of ice accumulation in the current cell is equal to the mass of water droplets entering the cell minus the mass of water leaving the cell. This can be expressed as

$$\dot{m}_{\mathrm{im}}+\dot{m}_{\mathrm{in}}-\dot{m}_{\mathrm{va}}-\dot{m}_{\mathrm{ou}}=\dot{m}_{\mathrm{so}} \tag{2}$$

where $\dot{m}_{\mathrm{im}}$ is the mass of water droplets hitting the unit per unit time; $\dot{m}_{\mathrm{in}}$ the mass of water flowing into the current cell from adjacent cells per unit time; $\dot{m}_{\mathrm{va}}$ the mass of water that evaporates per unit of time; $\dot{m}_{\mathrm{ou}}$ the mass of water flowing from the current cell into the adjacent cell per unit time; and $\dot{m}_{\mathrm{so}}$ the mass of all icing in the current unit time.

Therefore, the calculation principle of the anti-icing heat load is to increase the corresponding heat flux in the above freezing heat transfer process. This will ensure that, after the supercooled water droplets impact the surface of the aircraft, they will not freeze on the surface after the surface energy balances. The calculation principle of the anti-icing heat load bears resemblance to that of icing. In comparison to the heat transfer process of icing, the heat transfer term between ice and water and the overflow effect of water droplets between adjacent units are insignificant and can be ignored. As the surface temperature, in principle, remains at approximately 0 ℃ after applying the anti-icing heat flux to the surface unit, theoretically, no ice forms on the aircraft's surface[26], and the heat carried by the water droplets flowing into the adjacent unit is equal to the heat contained in the water droplets flowing out of the unit. The heat transfer on the surface unit is illustrated in Fig.2. In this case, the heat transfer model was simplified, and a calculation model for the anti-icing heat load was established. The calculation can be expressed as

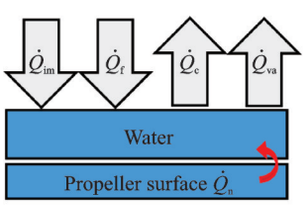

Fig.2 Diagram of energy transfer model in cell during anti-icing process

$$\dot{Q}_{\mathrm{n}}=\dot{Q}_{\mathrm{va}}-\dot{Q}_{\mathrm{im}}-\dot{Q}_{\mathrm{f}}+\dot{Q}_{\mathrm{e}} \tag{3}$$

In Eq.(3), the expression of each energy term is

$$\dot{Q}_{\mathrm{va}}=\dot{m}_{\mathrm{va}}\cdot L_{\mathrm{e}} \tag{4}$$

$$\dot{Q}_{\mathrm{im}}=\dot{m}_{\mathrm{im}}\cdot C_{\mathrm{f}}\cdot(T_{\mathrm{s}}-T_{\infty})+0.5\cdot\dot{m}_{\mathrm{im}}\cdot V^{2} \tag{5}$$

$$\dot{Q}_{\mathrm{f}}=h_{\mathrm{c}}\cdot A\cdot r_{\mathrm{c}}\cdot V^{2}/2C_{\mathrm{a}} \tag{6}$$

$$\dot{Q}_{\mathrm{e}}=h_{\mathrm{c}}\cdot A\cdot(T_{\mathrm{s}}-T_{\infty}) \tag{7}$$

where L_{e} is the latent heat of evaporation; C_{f} the specific heat capacity of water; h_{c} the convective heat transfer coefficient on the surface of the element; A the surface area of the element; r_{c} the recovery factor; C_{a} the specific heat capacity of air; and V the velocity of air at the surface. T_{s} and T_{∞} represent the unit surface and incoming flow temperature, respectively.

The unknown quantities that still exist in the above formula are $\dot{m}_{\mathrm{im}}$, $\dot{m}_{\mathrm{va}}$, and h_{c}. Therefore, the anti-icing heat load solution process is divided into three parts: $\dot{m}_{\mathrm{im}}$ calculation, $\dot{m}_{\mathrm{va}}$ h_{c} calculation, and anti-icing heat load calculation.

1.1 Calculations of $\dot{m}_{\mathrm{im}}$ and $\dot{m}_{\mathrm{va}}$

$\dot{m}_{\mathrm{va}}$ can be obtained by solving the airflow field. Meanwhile, and $\dot{m}_{\mathrm{im}}$ is obtained by solving the water droplet impact characteristics.

1.2 Calculation of airflow solution

The multiple reference frame (MRF) model[27] is used to approximate the incompressible Reynolds average Navier-Stokes (RANS) equation in the steady-state. To close the RANS equation set, a two-equation SST k-ω turbulence model is introduced[28]. The control equation is discretized by the finite volume method; the time term is the second-order implicit discretization, while the SIMPLE algorithm is used to calculate the flow field pressure, and the space discretization uses the central difference scheme.

1.3 Calculation of water droplet motion and impact characteristics

The calculation of the water droplet field on the surface of the propeller is based on the MRF model, and the mass and momentum conservation equa-

tions are solved using Euler's method. The equations are

$$\frac{\partial \alpha}{\partial t} + \nabla(\alpha V_{\mathrm{d}}) = 0 \tag{8}$$

$$\frac{\partial(\alpha V_{\mathrm{d}})}{\partial t} + \nabla\cdot(\alpha V_{\mathrm{d}}^2) + 2\alpha\omega^2 \times r + \omega \times V_{\mathrm{d}} = \frac{C_{\mathrm{D}} Re_{\mathrm{d}}}{24K}\alpha(V_{\infty} - V_{\mathrm{d}}) + \alpha(\rho_{\mathrm{d}} - \rho_{\mathrm{a}})g \tag{9}$$

where α and V_{d} represent the average field value of the particle concentration and velocity of water droplets in the air, respectively. C_{D} is the droplet drag coefficient, Re_{d} the Reynolds number for water droplets, and K the inertia factor[29]. The equations for C_{D} and Re_{d} are

$$C_{\mathrm{D}} = \frac{Re_{\mathrm{d}}}{24}(1.0 + 0.197 Re_{\mathrm{d}}^{0.63} + 2.6 \times 10^{-4} Re_{\mathrm{d}}^{1.38}) \tag{10}$$

$$Re_{\mathrm{d}} = \frac{\rho_{\mathrm{a}} \mathrm{MVD} |V_{\infty} - V_{\mathrm{d}}|}{\mu_{\mathrm{a}}} \tag{11}$$

where MVD is the median volume diameter of the water droplet.

The water droplet collection coefficient β can be determined by the velocity vector and water content, and the equation is

$$\beta = \frac{\alpha}{\mathrm{LWC}} \frac{|V_{\mathrm{d}} \cdot \boldsymbol{n}|}{|V_{\infty}|} \tag{12}$$

where LWC is the droplet volume fraction of the far-field, V_{∞} the incoming flow speed, and $\boldsymbol{n}$ the unit normal vector at the collision point of the object surface.

The total mass of the water droplet impact in the object plane unit can be expressed as

$$m_{\mathrm{im}} = \beta \cdot \mathrm{LWC} \cdot V_{\infty} \tag{13}$$

1.4 Calculation of convective heat transfer coefficient

The surface temperature gradient distribution and heat flux can be determined through flow field calculations using the SST k-ω turbulence model with wall roughness correction. However, the distribution of convective heat transfer coefficient obtained by this method at stagnation point is not accurate[30], thus requiring correction using an empirical formula. To address this, the blade surface is divided into two sections. The convective heat transfer coefficient near the stagnation point is approximately calculated according to the cylindrical formula, and the convective heat transfer coefficient of the rear part is approximately calculated using the flat plate formula.

When the airflow passes through the stagnation point, the front edge is approximated as a circle, and the surface convective heat transfer coefficient is expressed as[31]

$$h_{\mathrm{c}} = 0.063 \frac{\lambda}{D} Re_{\mathrm{D}}^{0.8} Pr^{1/3} \tag{14}$$

where D is the diameter of the circle and Pr the laminar Prandtl number.

When the air flows around the rear area, the surface convective heat transfer coefficient is calculated using plate convection, which can be expressed as[31]

$$h_{\mathrm{c}} = 0.029\,6 \times \frac{\lambda}{S} Re_X^{0.8} Pr^{1/3} \tag{15}$$

where S is the distance to the leading edge point; λ the thermal conductivity of air, which is related to the temperature, and can be estimated by the following formula

$$\lambda = 2.524 \times 10^{-2} \left(\frac{T_{\mathrm{f}}}{288}\right)^{0.8} \tag{16}$$

where T_{f} is the absolute temperature. Based on the values of $\dot{m}_{\mathrm{im}}$, $\dot{m}_{\mathrm{va}}$, and h_{c} obtained above, Eqs.(4—7) are introduced into Eq.(3) to solve the anti-icing heat load $\dot{Q}_{\mathrm{n}}$.

2 Validation

We utilized in-house software capable of simulating the 3D rotation effect, icing shapes, and the anti-icing heat load problem to perform calculations for this study. The reliability of the software was verified by comparing the calculated ice shapes with experimental results, a verification method also employed in Ref.[32]. The reasons are as follows: Firstly, the principle of anti-icing heat load calculation only considers the effect of thermodynamic calculation; however, the calculation of icing needs to consider the thermodynamic effects, overflow of water between surface elements, phase change of water, and change of surface ice shape. The icing calculation has already encompassed the calculation of the anti-icing heat load. Secondly, accurately mea-

suring the anti-icing heat load from icing wind tunnel test data is challenging. Additionally, documentation on anti-icing heat load specifically for propellers is scarce. Thirdly, the icing experiment can be directly conducted to obtain the corresponding ice shape, which is convenient for comparison with simulation results. Therefore, to verify the reliability of the calculation method of a 3D propeller surface anti-icing heat load, this study compares the icing behavior of fixed wings and wind turbine blades.

To verify the reliability of the algorithm for calculating horn ice and streamwise ice, NACA0012 airfoil was selected as the verification model, and the results of two groups of examples, V_∞ = 129.46 m/s, T = −12.6 ℃, p = 90 749 Pa, LWC = 0.5 g/m^3, MVD = 20 μm, t = 360 s, and V_∞ = 64.73 m/s, T = −12.6 ℃, p = 90 749 Pa, LWC = 0.5 g/m^3, MVD = 20 μm, t = 600 s, were compared with the data in Ref.[29]. As shown in Fig.3, the ice shape curves were well fitted.

In this study, the reliability of the 3D rotary icing calculation was verified by comparing the icing geometry data in Ref.[33]. Ice is formed at the leading edge of the spreading direction, z = 20 m, z = 30 m, and the blade tip is shown in Fig.4. The calculated results are shown in Fig.5, and the environmental parameters are estimated as follows: T = −5.8 ℃, LWC = 0.5 g/m^3, and MVD = 20 μm. The conditions for accurate measurement were V_∞ = 8 m/s and a wind turbine speed of 17 r/min. The actual thickness of icing in these three parts can be obtained through measurement. Since the ice shape curve cannot be accurately measured in the field test site, the reliability of the method can only be verified by comparing the experimental data of the ice shape thickness and the calculation results, as shown in Table 1. There are some errors when comparing the results, the reasons for these errors are as follows: (1) The calculation conditions are measured on-site, and there may be measurement errors in environmental parameters, such as liquid water content and water droplet diameter; (2) the ice being measured is not fresh as it is melted; (3) the ice formation calculation results corresponded imprecisely to the actual ones. However, in general, the ice thickness in the calculation and the actual

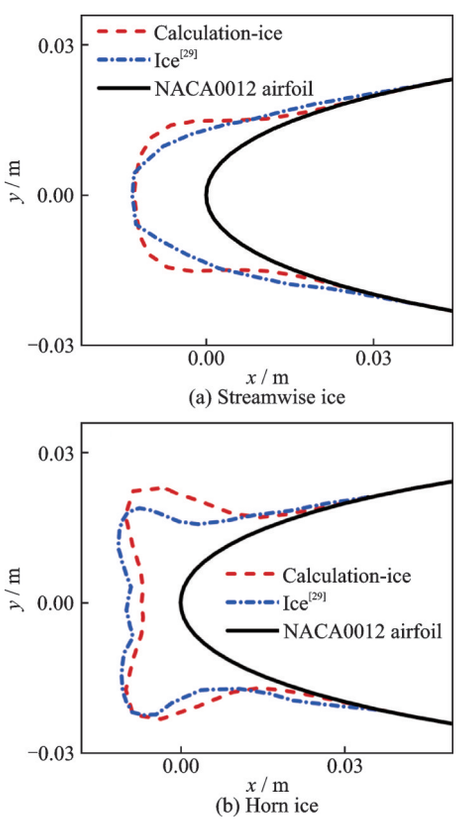

Fig.3 Computed ice shape on NACA0012 airfoil

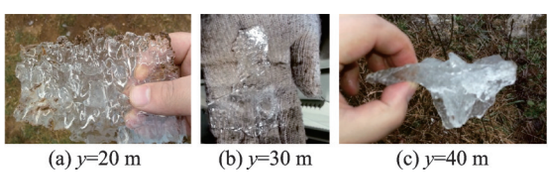

Fig.4 Ice at each spanwise location of blade

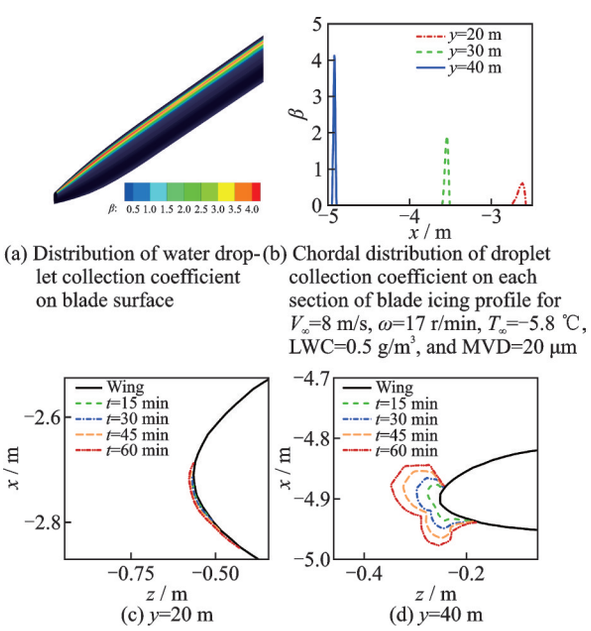

(a) Distribution of water droplet collection coefficient on blade surface (b) Chordal distribution of droplet collection coefficient on each section of blade icing profile for V_∞=8 m/s, ω=17 r/min, T_∞=−5.8 ℃, LWC=0.5 g/m^3, and MVD=20 μm

Fig.5 Calculation results of icing on wind turbine blade

thickness are basically the same in magnitude, and the distribution trend is in line with the expected pattern, indicating that the proposed ice calculation method considering the rotation effect is reliable.

Table 1 Predicted and actual thicknesses of ice (y represents the spanwise position of the blade)

Ice location	Predicted ice thickness/mm	Actual ice thickness/mm	Relative error/%
$y = 40$ m	18.8	13.4	28.70
$y = 30$ m	9.6	7.5	21.80
$y = 20$ m	3.5	4.2	20.00

3 Results and Discussion

Using a typical propeller aircraft blade, the study investigated the anti-icing heat load of the propeller under a typical working environment. The distribution pattern of the anti-icing heat load on the surface of the propeller is also analyzed. The basic calculation conditions are as follows: The angle of attack α is 0°, $p = 101\ 325$ Pa, $V_\infty = 90$ m/s, $T_\infty = -10$ ℃, LWC = 0.5 g/m^3, and MVD = 20 μm. The effects of these five parameters, such as angle of attack, liquid water content, water droplet size, incoming flow speed, and air temperature, are studied, respectively.

The model used in the calculation is shown in Fig.6. The propeller has a diameter of 3.8 m and rotates at a speed of 660 r/min. The mounting angle of the blade on the propeller fairing is 42.4°. Fig.7 shows the grid division of the densified area and the surface grid distribution of a typical area. To verify grid independence, 11 groups of propeller models with different grid numbers are calculated, including 3, 3.56, 3.72, 3.87, 4.18, 4.4, 4.99, 5.27, 7.5, 8.6, and 10 million grids, under the flow conditions of an incoming flow speed of 90 m/s, a rotation speed of 660 r/min, a pressure of 101 325 Pa, and a temperature of 263.15 K. The distribution of the influence of grid numbers on propeller thrust is shown in Fig.8. Finally, 4.99 million grid cells are selected for the calculation. The anti-icing heat load of the propeller under basic conditions ($V_\infty = 90$ m/s, $\alpha = 0°$, MVD = 20 μm, LWC = 0.5 g/m^3, $T_\infty = -10$ ℃) is analyzed. As shown in Fig.9, the anti-icing heat load and droplet impact zone distribution on the surface of the propeller are mainly concentrated on the leading edge of the blade, with a maximum value of 9.5 kW/m^2. As shown in Figs.10(a, b), the spanwise position of the cross-section are $z = 1.4$ m. It is worth noting that the curve corresponding to the leading edge of the blade has an obvious lower concave shape, which corresponds to the droplet runback phenomenon. This is because the large amount of kinetic energy carried by the droplet. Fig.10(c) shows the propeller blade spanwise coordinate direction. Fig.10(d) shows the spanwise distribution of anti-icing heat loads on propeller blades, wind turbine blades[22] ($V_\infty = 11.4$ m/s, $\alpha = 0°$, MVD = 20 μm, $T_\infty = -10$ ℃, $\omega = 12.1$ r/min), and fixed

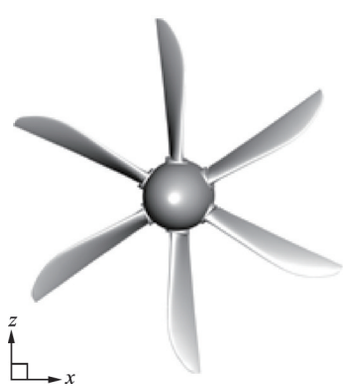

Fig.6 Calculation model

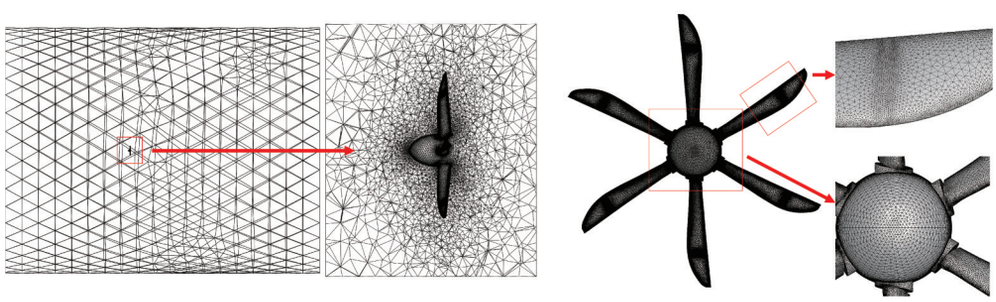

Fig.7 Calculation grid

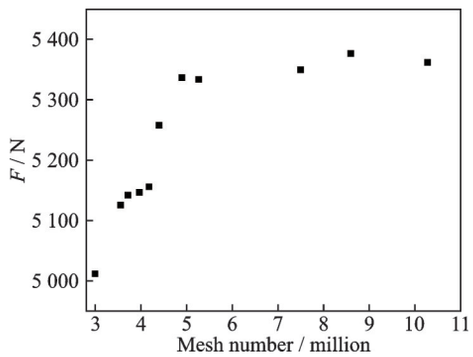

Fig.8 Relationship between mesh number and propeller thrust

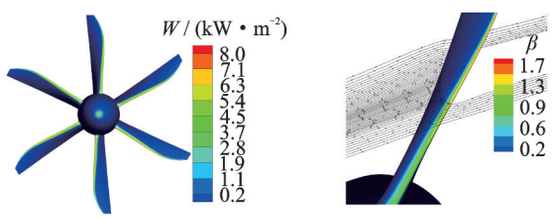

(a) Profile of anti-icing heat load (b) Profile of water droplet collection coefficient

Fig.9 Anti-icing heat load and water droplet collection coefficient profiles for $V_\infty = 90$ m/s, $\alpha = 0°$, MVD = 20 μm, LWC = 0.5 g/m^3, $T_\infty = -10$ ℃

wings[34] (V_∞ =89.4 m/s, $\alpha = 0°$, MVD = 20 μm, $T_\infty = -21.8$ ℃). Evidently, it can be seen that the anti-icing heat load along the spanwise direction of the fixed-wing surface changes little, but the spanwise distribution of the other two increases first and then decreases. The root cause is the rotation effect, which results in a first-order linear increase in velocity along the spanwise direction. In contrast, the anti-icing heat load increases first-order linearly along the spanwise direction due to the increase of water droplet collection. It is well-known that the droplet collection coefficient is positively correlated with velocity[35]. Meanwhile, the kinetic energy of the droplets and aerodynamic heat energy are proportional to the square of air velocity, as shown in Eqs.(5, 6), which will reduce the anti-icing heat load.

Therefore, in the inner section of the blade span, water droplet collection is the main factor of the anti-icing heat load due to the low wind speed. However, in the outer section of the blade span, the kinetic energy of the water droplets and aerodynamic heat energy become the main factors affecting the anti-icing heat load due to the large wind speed. This eventually leads to a phenomenon that the anti-icing heat load increases first and then decreases along the spanwise direction. However, it should be noted that the incoming flow speed of a wind turbine in a working environment is approximately 15 m/s, and the speed is approximately 18 r/min, as shown in Eq.(17). The impact of water kinetic energy and aerodynamic heat energy is extremely limited in this case. Therefore, water droplet collection plays a dominant role in wind turbine icing. Additionally, the reduction in blade section lengths decreases the anti-icing heating power at the blade tip of the wind turbine[22]. Thus, the anti-icing heat load gradually increases with the wind turbine blade span and decreases towards the tip, as depicted in Fig.10(d).

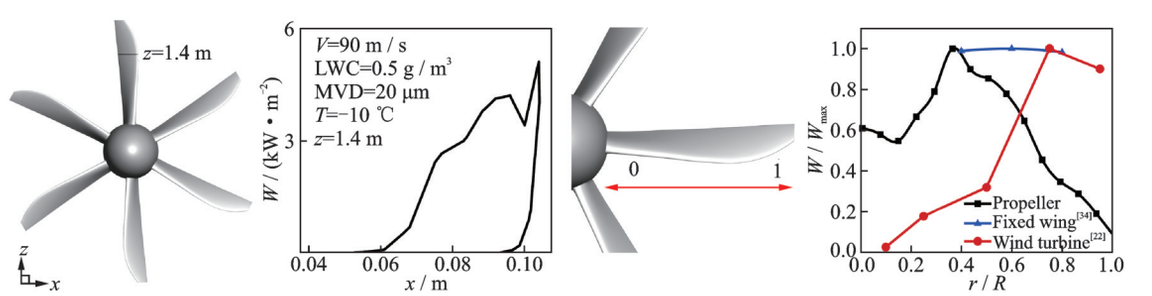

(a) Schematic diagram of spanwise location position of z=1.4 m (b) Anti-icing heat load distribution on the cross-section at z=1.4 m (c) Schematic diagram of span direction (d) Distribution curves of anti-icing anti-icing heat load in blade spanwise

Fig.10 Distribution of anti-icing heat load on the blade cross-section at z=1.4 m and spanwise under the basic conditions

$$V = \sqrt{V_\infty^2 + \left(\frac{2\pi\omega l}{60}\right)^2} \tag{17}$$

where l is the span length.

3.1 Effect of different angles of attack

The distribution law of the anti-icing heat load on the propeller blade surface is analyzed by compar-

ing the results of seven sets of calculation examples under different angles of attack. As shown in Fig.11 (a), the positive and negative angles of attack have little effect on the anti-icing heat load distribution on the surface. When the angle of attack is 10°, the anti-icing heat load on the blade leading edge decreases by 3.3% compared with that at an angle of attack of 0°. With the increase in the absolute value of the angle of attack, the anti-icing heat load decreases slightly. This is because as the angle of attack increases, the effective speed of the water droplet impact decreases, reducing the amount of water droplets collected per unit time on the propeller surface. Additionally, the propeller has a symmetric structure about its center, and the angle of the incoming flow of a single blade always switches between positive and negative during rotation. Hence, the effect of positive and negative angles of attack on the anti-icing heat load is weakened.

However, the angle of attack significantly affects the anti-icing load on fixed-wing surfaces[36]. Fig.11(b) shows the distribution results of the anti-icing heat load on the fixed-wing surface in Ref.[37] (V_∞ = 131.38 m/s, MVD = 20 μm, T_∞ = −4.5 ℃, LWC = 1.0 g/m^3). When the angle of attack is 4°, the anti-icing heat load on the leading edge of the fixed wing reaches its maximum value, which increases by 22% compared with that at 0°. With the increase in the angle of attack, the anti-icing heat load on the lower surface of the fixed wing increases, while that on the upper surface decreases. Furthermore, as the angle of attack increases, the stagnation point moves down. The incoming air slows down as it flows up the surface and speeds up as it flows down the surface. Therefore, the convective heat transfer coefficient of the upper surface decreases, and that of the lower surface increases. Compared with the propeller, the angle of attack has a more significant ice protection effect for the fixed wing. The main reason for this difference is that the rotation effect can weaken the influence of asymmetric parameters.

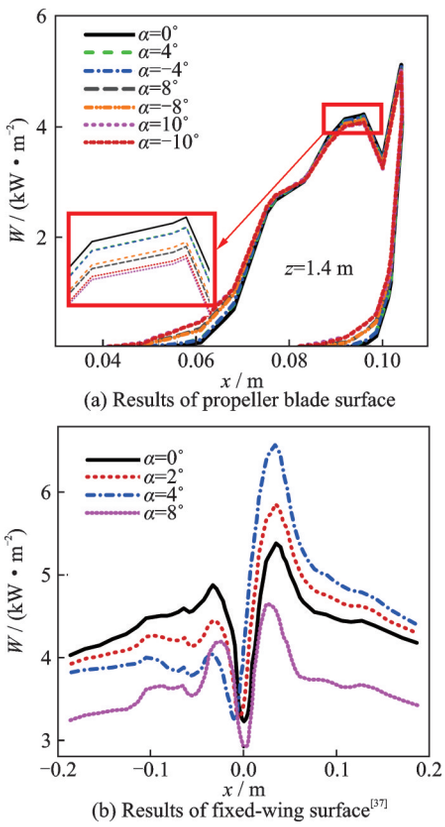

Fig.11 Calculation results of anti-icing heat load for various angles of attack on propeller blade surface and results of fixed-wing surface from Ref.[37]

3.2 Effect of different LWCs and air temperatures

To study the influence of LWC and T on the anti-icing heat load, the results of eight sets of calculation examples under different conditions of LWC and T are compared. As shown in Figs.12(a, b), as the LWC increases or T decreases, the surface heat load increases proportionally. When the LWC in the air increases, the total amount of water droplets collected on the surface of the propeller increases, as shown in Eq.(13), causing the surface to require more heat to prevent icing. Moreover, as shown in Eqs.(3, 5, 7), when the temperature drops, the convection heat transfer $\dot{Q}_c$ increases, and the energy carried by the droplet $\dot{Q}_{im}$ decreases, which directly results in a linear increase in the anti-icing heat load $\dot{Q}_n$, as shown in Fig.12(c). In addition, the effect of T on the fixed wing[37] is similar to that on the rotating machine, as shown in Fig.12

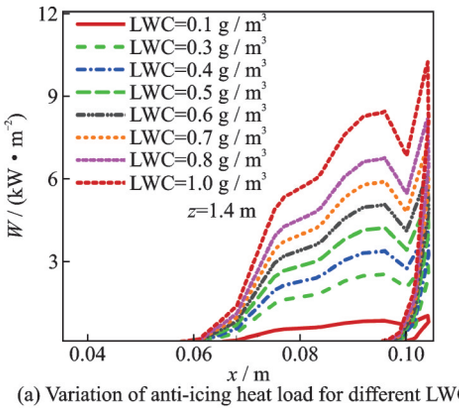

(a) Variation of anti-icing heat load for different LWCs

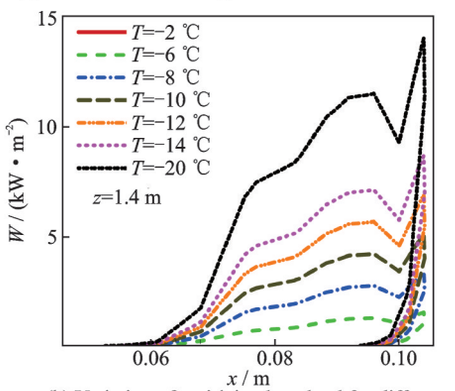

(b) Variation of anti-icing heat load for different temperature on propeller blade surface

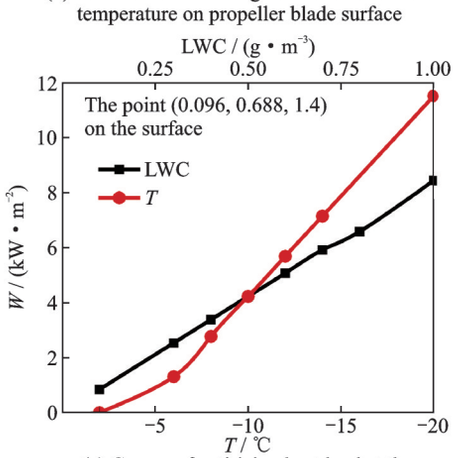

(c) Curves of anti-icing heat load at the point with temperature and LWC

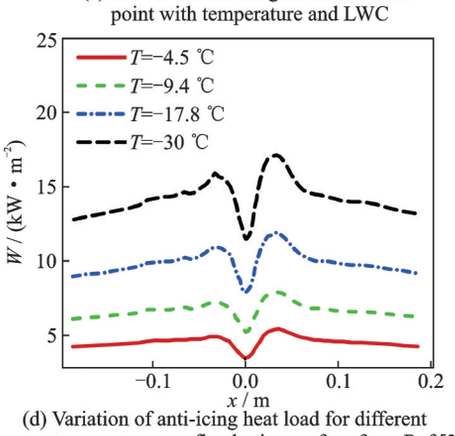

(d) Variation of anti-icing heat load for different temperatures on fixed-wing surface from Ref.[37]

Fig.12 Calculation results of anti-icing heat load for various LWCs and temperature on propeller blade surface and results of fixed-wing surface from Ref.[37]

(d). This is because the variation in T has little effect on droplet inertia, air shear force, and flow field pressure[38]; hence, the droplet impact trajectory remains the same, and the impact range remains unchanged.

3.3 Effect of different MVDs

To study the influence of MVD on the anti-icing heat load, the results of seven sets of calculation examples under different MVD conditions are compared. As shown in Fig.13(a), as the water droplet size increases, the anti-icing heat power and surface area of the propeller increase. An increase in droplet size will enhance the efficiency of droplet collection[39] and impact area[40]. However, as the MVD continues to increase, the increment of the droplet collection coefficient and anti-icing heat load decreases, as shown in Fig.13(b). This is because the inertia force plays a dominant role in the impact process, and the influence of the aerodynamic force on droplets decreases[19]. As a result, it becomes more difficult for the water droplets to deviate from their original trajectories[41], leading to a stabilization of the droplet collection coefficient. The distribution of the anti-icing heat load is related to the droplet collection coefficient; thus, the anti-icing heat load tends to stabilize with an increase in MVD. The influence trend of MVD on the surface of a fixed wing and a propeller is similar, although the degree of influence varies. This is because the effect of droplet size is based on the speed, and propellers, wind turbines, and fixed-wing aircraft have different speed distributions on their surfaces due to different operating conditions.

3.4 Effect of different incoming flow speeds

To study the influence of the incoming flow speed on the anti-icing heat load and range, the results of eight sets of calculation examples under different conditions of incoming flow speed are compared. In the eight sets of calculation examples, the incoming flow velocity is 70, 90, 100, 110, 130, 140, 150, and 200 m/s, respectively, and the corresponding rotation speed of the incoming flow speed is 513, 660, 733, 806, 953, 1026, 1 099, 1 465 r/min, respectively. As shown in Figs.14(a,

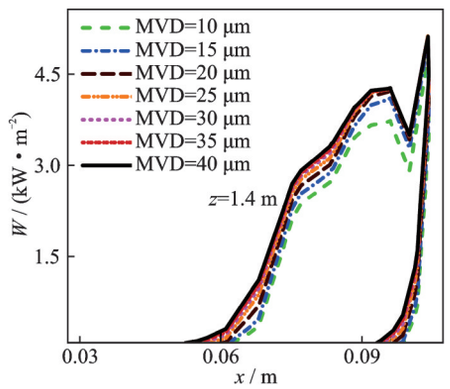

(a) Variation of anti-icing heat load for different water droplet diameters at V_∞=90 m/s, α=0°, LWC=0.5 g/m^3, T_∞=−10 ℃, z=1.4 m

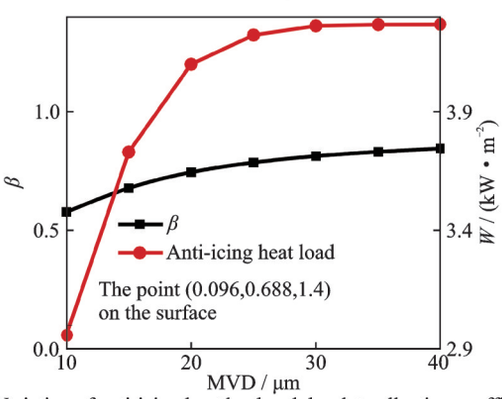

(b) Variation of anti-icing heat load and droplet collection coefficient with water droplet diameters at the point (0.096, 0.688, 1.4)

Fig.13 Calculation results of anti-icing heat load for various water droplet diameters on propeller blade surface

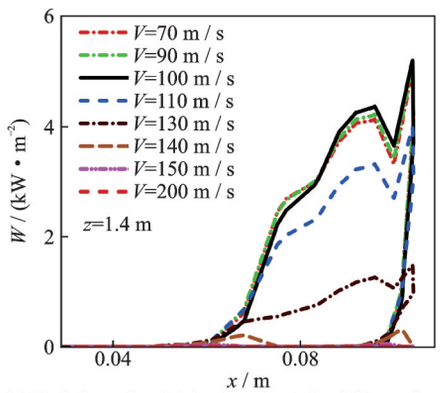

(a) Variation of anti-icing heat load for different incoming flow speeds at α=0°, MVD=20 μm, LWC=0.5 g/m^3, T_∞=−10 ℃, z=1.4 m on the propeller blade surface

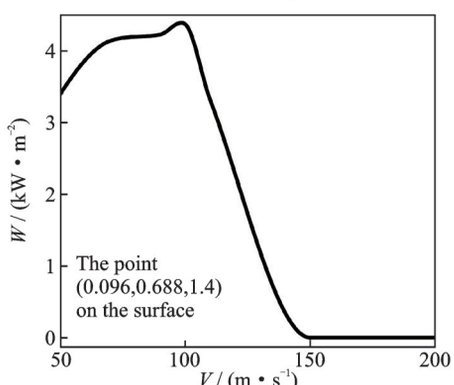

(b) Anti-icing heat load curve as the incoming flow speed at the point (0.096, 0.688, 1.4)

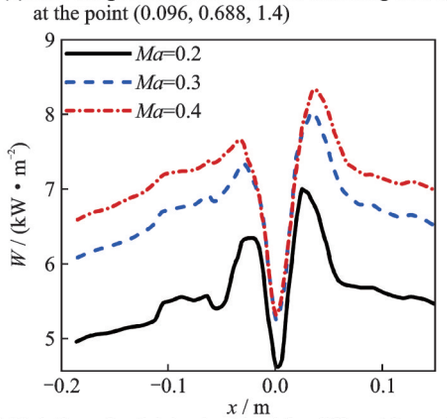

(c) Variation of anti-icing heat load for different incoming flow speeds on fixed-wing surface from Ref.[37]

Fig.14 Calculation results of anti-icing heat load for various incoming flow speeds on propeller blade surface and results of fixed-wing surface from Ref.[37]

b), as the incoming flow speed increases, both the value and range of the anti-icing heat loads increase and then decrease. When the incoming flow speed reaches 100 m/s (i.e., the local speed on the surface is 139 m/s), the required anti-icing heat load on the surface reaches its maximum value. Due to the increase in the incoming flow speed, the surface of the propeller collects more water per unit time, as indicated by Eq.(13). From Eqs.(4—6, 11—13), $\dot{Q}_f$, $\dot{Q}_{im}$ and $\dot{Q}_c$ can be reduced to Eqs.(17—19), respectively. Additionally, the flow in the boundary layer of the blade surface is accelerated[34], which increases the convective heat transfer $\dot{Q}_c$[42], the skin friction heat $\dot{Q}_f$, and the energy carried by the droplet $\dot{Q}_{im}$ according to Eqs.(18—20). The skin friction heat $\dot{Q}_f$ and the energy carried by the droplet $\dot{Q}_{im}$ are highly sensitive to the velocity, and they increase significantly with the increase of velocity. When the speed is high, the skin friction heat $\dot{Q}_f$ and the energy carried by the droplet $\dot{Q}_{im}$ play a dominant role in influencing the anti-ice heat load. Therefore, when the speed exceeds 100 m/s, the anti-icing heat load decreases. When the speed reaches 150 m/s (i.e., the local speed on the surface is 178 m/s), the anti-icing heat load decreases to 0.

$$\dot{Q}_{\mathrm{f}} = ab\frac{r_{\mathrm{c}}}{2C_{\mathrm{a}}}V^{2.8} \tag{18}$$

$$\dot{Q}_{\mathrm{im}} = 0.5\alpha\frac{|V\cdot\boldsymbol{n}|}{V_{\infty}}V^{4} - c\alpha\frac{|V\cdot\boldsymbol{n}|}{V_{\infty}}V \tag{19}$$

$$\dot{Q}_{\mathrm{c}} = abV^{0.8} \tag{20}$$

where $a = 0.063\frac{\lambda}{D}\left(\frac{\rho D}{\mu}\right)^{0.8}Pr^{1/3}$, $b = A(T_{\mathrm{s}} - T_{\infty})$, $c = C_{\mathrm{f}}(T_{\mathrm{s}} - T_{\infty})$.

Vukits[43] reported that at true flow speeds above 430 knots at sea level or 475 knots at 6.096 km, the water droplets on the surface no longer freeze. This is because the energy carried by the droplet $\dot{Q}_{\mathrm{im}}$ and skin friction $\dot{Q}_{\mathrm{f}}$ provide enough heat to prevent freezing. In the case of wind turbines, the incoming flow speed in the working environment is approximately 15 m/s, which is very small compared with the tangential speed of the blade tip. Therefore, the influence on the wind turbine is not significant[23]. In the case of fixed-wing aircraft, the wind speed changes minimally in the spanwise direction, resulting in little variation in the anti-icing heat load related to wind speed along the spanwise direction. The presented by Guan[37] shows that the increase of speed will also increase the anti-icing heat load of the fixed wing, as shown in Fig.14(c). Similarly, the anti-icing heat load on the fixed-wing surface also drops to 0 at speeds above approximately 200 m/s.

4 Discussion of Anti-icing of Range and Power of Propeller Surface

To provide effective reference data for practical applications, it is necessary to choose calculation conditions that closely correspond to actual flight conditions. Therefore, the typical conditions are chosen based on the continuous maximum icing conditions specified in Appendix C of the CCAR-25.

4.1 Discussion of anti-icing range

Based on the maximum continuous icing conditions specified in Appendix C of the CCAR-25 and actual air temperature, a quantitative analysis is conducted on the distribution range of the anti-icing heat load with V_{∞} = 100 m/s, MVD = 40 μm, LWC = 0.06 g/m^3, T_{∞} = −20 ℃, and α = 10°. As shown in Fig.15, the anti-icing area is concentrated at the leading edge of the blade, and the chordwise anti-icing limit decreases as the span distance extends. The maximum values of the upper limit S_{u} and the lower limit S_{l} are found in the root area of the blade, with values of 12.1 and 6.4%, respectively. It is worth noting that in Ref.[21], the anti-icing area of wind turbine blades increases in the spanwise direction, which differs from propellers. Although they are both rotating machines, at low speeds, they tend to rely more on the anti-icing heat flux to resist ice contamination.

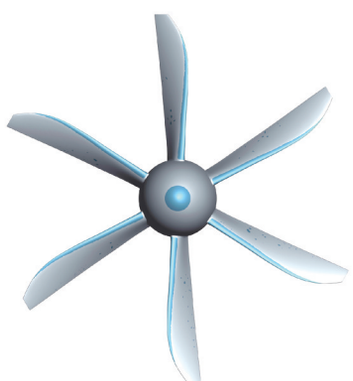

(a) Anti-icing area profile for V_{∞}=100 m/s, MVD=40 μm, LWC=0.06 g/m^3, T_{∞}=−20 ℃, and α=10°

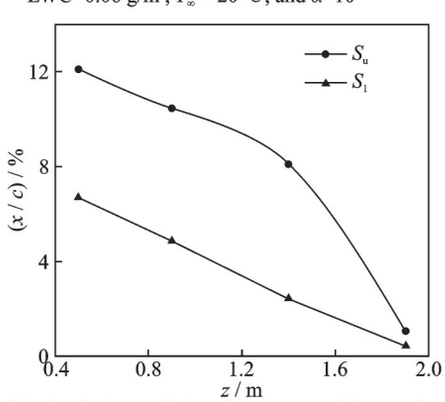

(b) Chordwise anti-icing limit curves with span distance

Fig.15 Anti-icing area on the propeller blade under typical conditions

4.2 Discussion of anti-icing power

According to the maximum continuous icing conditions specified in Appendix C of the CCAR-25, there is an inversely proportional relationship

between LWC and T; however, severe icing occurs in the range of −8 ℃ to −10 ℃[41]. Therefore, the conditions of V_∞ = 100 m/s, MVD = 15 μm, LWC = 0.6 g/m^3, T_∞ = −10 ℃, and α = 0° are selected to perform a quantitative analysis of the anti-icing power on the propeller surface. As shown in Fig.16, the maximum anti-icing heat load at the blade root(z = 1.0 m) is 9.5 kW/m^2. Furthermore, the heat load on the entire propeller surface is obtained through integration, and the anti-icing power required for a single propeller is 1.96 kW.

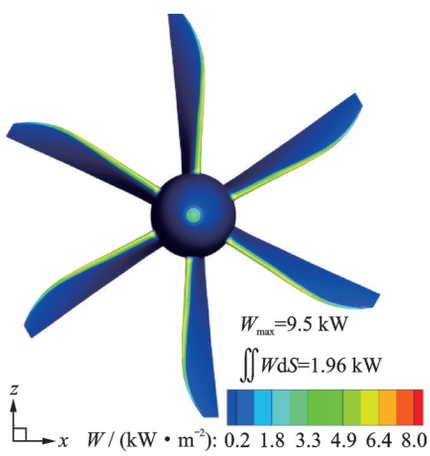

Fig.16 Anti-icing heat load distribution on the propeller surface in severe icing environment

In summary, the anti-icing area on the propeller surface should be concentrated on the leading edge of the blade, with a maximum limit of 12.1% along the chordwise upward direction, a maximum limit of 6.7% along the chordwise downward direction, and a maximum anti-icing range of 85% along the span. The maximum anti-icing power should be 9.5 kW/m^2, and the anti-icing power of the single propeller should surpass 1.96 kW. In practical engineering applications, a certain margin is usually reserved to increase the power by calculating the anti-icing power.

5 Conclusions

When the propeller-driven aircraft operates in icing conditions, ice accumulates on the leading edge of the propeller blades. In this study, the anti-icing heat load on the propeller surface is calculated, the results are compared with those of wind turbines and fixed wings in the literature, and the following conclusions are drawn:

(1) The heat load on the propeller is primarily concentrated at the leading edge of the blade. The anti-icing range along the chordwise upward direction is 12.1%, while along the chordwise downward direction it is 6.7%. This range decreases with the spanwise direction. The maximum anti-icing power is 9.5 kW/m^2, and the power required for a single propeller is 1.96 kW. The heat load value increases first and then decreases along the span direction. As the incoming flow speed increases, the anti-icing power and range increase first and then decrease. When the local speed on the blade surface is approximately close to 139 m/s, the highest anti-icing power is required. The effects of LWCs, MVDs, and temperature on the propeller exhibit a linear relationship. An increase in LWCs or MVDs or a decrease in temperature, leads to an increase in the anti-icing heat flux.

(2) The distribution of the anti-icing heat load on the surface of a high-speed rotating propeller is first studied. The obtained results differ from similar existing research reports on fixed wings or wind turbines. The main differences are observed in the spanwise distribution of the anti-icing heat load and the influence of the angle of attack and incoming flow speed.

(3) The results can provide a scientific explanation for anti-icing of the propeller and provide a reference for installing anti-icing devices in high-speed rotating machinery.

References

[1] CAO Y, CHAO M, QIANG Z, et al. Numerical simulation of ice accretions on an aircraft wing[J]. Aerospace Science and Technology, 2012, 23(1): 296-304.

[2] EBRAHIMI A, HAJIPOUR M, HASHEMINASAB H. Experimental investigation on the aerodynamic performance of NLF-0414 iced-airfoil[J]. Journal of

Applied Fluid Mechanics, 2016, 9(2): 587-592.

[3] XIAN Y, QIANG W, CONGCONG C, et al. Prediction model of aircraft icing based on deep neural network[J]. Transactions of Nanjing University of Aeronautics & Astronautics, 2021, 38(4): 535-544.

[4] MILLER T L, KORKAN K D, SHAW R J. Analytical determination of propeller performance degradation due to ice accretion[J]. Journal of Aircraft, 1987, 24(11): 768-775.

[5] LI L K, LIU Y, TIAN L C, et al. An experimental study on a hot-air-based anti-/de-icing system for aero-engine inlet guide vanes[J]. Applied Thermal Engineering, 2020, 167: 114778.

[6] DONG W, ZHU J, ZHENG M, et al. Thermal analysis and testing of a cone with leading edge hot air anti-icing system[C]//Proceedings of the 52nd AIAA Aerospace Sciences Meeting. Maryland: AIAA, 2013: 1-13.

[7] LV Qing, NING Liwei, YAN Xi, et al. Analysis of wind turbine blade de-icing based on gas and heat method[J]. Journal of Hunan Institute of Engineering, 2016, 27(2): 28-32. (in Chinese)

[8] LYU Y, ZHANG J, SHAN Y, et al. The experimental investigation of impinging heat transfer of pulsation jet on the flat plate[J]. ASME Journal of Heat and Mass Transfer, 2018, 140(12): 122202.

[9] POURBAGIAN M, HABASHI W G. Aero-thermal optimization of in-flight electro-thermal ice protection systems in transient de-icing mode[J]. International Journal of Heat and Fluid Flow, 2015, 54: 167-182.

[10] URANAI S, FUKUDOME K, MAMORI H, et al. Numerical simulation of the anti-icing performance of electric heaters for icing on the NACA 0012 airfoil[J]. Aerospace, 2020, 7(9): 123.

[11] SABATIER J, LANUSSE P, FEYTOUT B, et al. Ice accretion detection and anti-icing/deicing systems for wind turbine blades[C]//Proceedings of the 14th International Conference on Informatics in Control, Automation and Robotics (ICINCO). Madrid: Lecture Notes in Electrical Engineering, 2017: 641-663.

[12] MU Z, SHEN X, LIN G, et al. Simulation of unsteady electro-thermal de-icing process of anisotropic composite skin[J]. IET Conf Proc (UK), 2020, 2020(3): 852-862.

[13] BU Xueqin, LIN Guiping. Predictions of collection efficiency and anti-icing surface temperature[J]. Journal of Beijing University of Aeronautics Astronautics, 2007, 33(10): 1182-1185. (in Chinese)

[14] FENG Lijuan, QIN Na, YI Xian. Aero-engine inlet anti-icing system power requirement simulation definition methodology investigation[J]. Aeronautical Computing Technique, 2017, 47(4): 14-17. (in Chinese)

[15] ZHAO Yong, YANG Xinliang. Impingement characteristics and anti-icing heat load calculation of certain tailplane[J]. Journal of Aerospace Power, 2012, 27(11): 2401-2407. (in Chinese)

[16] VILLALPANDO F, REGGIO M, ILINCA A. Prediction of ice accretion and anti-icing heating power on wind turbine blades using standard commercial software[J]. Energy, 2016, 114: 1041-1052.

[17] CHANG S, LENG M, YANG B, et al. Study of the minimum anti-icing energy based on icing limit state [C]//Proceedings of the 45th AIAA Thermophysics Conference. Dallas: AIAA, 2015: 1-8.

[18] BU X, YANG R, YU J, et al. New method for calculation of anti-icing heat loads[J]. Energy and Power Engineering, 2013, 5(4): 493-497.

[19] WANG Z. Calculation of airfoil anti-icing heat load in SLD conditions[C]//Proceedings of the 22nd AIAA Computational Fluid Dynamics Conference. Dallas: AIAA, 2015.

[20] HANN R, ENACHE A, NIELSEN M, et al. Experimental heat loads for electrothermal anti-icing and de-icing on UAVs[J]. Aerospace, 2021, 8(3): 83.

[21] REID T, BARUZZI G, OZCER I, et al. FENSAP-ICE simulation of icing on tind turbine blades, Part 2: Ice protection system design[C]//Proceedings of the 51st AIAA Aerospace Sciences Meeting Including the New Horizons Forum & Aerospace Exposition. Grapevine: AIAA, 2013.

[22] YASSIN K, STOEVSANDT B, PEINKE J. Numerical estimation of anti-icing heating powerfor NREL 5 MW wind turbine blades in coldclimate[J]. Journal of Physics Conference Series, 2020. DOI: 10.1088/1742-6596/1618/5/052075.

[23] HANN R, NEUMANN S O, MILLER A, et al. Thermal analysis of a heated rotor blade for wind turbines[C]//Proceedings of Winterwind 2012 International Wind Energy Conference. [S.l.]: Institute of Aerospace Thermodynamics, 2012.

[24] BATTISTI L, FEDRIZZI R, SAVIO S D, et al. Influence of the type and size of wind turbines on anti-ic-

ing thermal power requirements for blades[C]//Proceedings of Euromech Colloquium 464b on Wind Energy. Oldenburg: Wing Energy, 2007: 305-308.

[25] NATERER G F. Temperature gradient in the unfrozen liquid layer for multiphase energy balance with incoming droplets[J]. ASME Journal of Heat and Mass Transfer, 2003, 125(1): 186-189.

[26] ZENG Feixiong, MAO Handong, ZHANG Ruchen. Modeling and simulation of civil aircraft nacelle anti-ice performance analysis[J]. Journal of Nanjing University of Aeronautics & Astronautics, 2022, 54(6): 1108-1113. (in Chinese)

[27] TABATABAEI N, CERVANTES M J, TRIVEDI C. Investigation of the numerical methodology of a model wind turbine simulation[J]. Journal of Applied Fluid Mechanics, 2018, 11(3): 527-544.

[28] ELGHAZALI A F, DOL S S. Aerodynamic optimization of unmanned aerial vehicle through propeller improvements[J]. Journal of Applied Fluid Mechanics, 2020, 13(3): 793-803.

[29] CEBECI T, CHEN H, ALEMDAROGLU N. Fortified LEWICE with viscous effects[J]. Journal of Aircraft, 1991, 28(9): 564-571.

[30] YANG Shenghua, LIN Guiping, SONG Xin. Comparative study on the numerical computation of convective heat transfer over rough syrface[J]. Journal of Aerospace Power, 2011, 26(3): 570-575. (in Chinese)

[31] BOND T, ANDERSON D. Manual of scaling methods: NASA/CR-2004-212875[R]. [S.l.]: NASA, 2004.

[32] ZHU Chengxiang, FU Bin, SUN Zhiguo, et al. Calculation of wind turbine anti-icing heat load[J]. Journal of Nanjing University of Aeronautics & Astronautics, 2011, 43(5): 701-706. (in Chinese)

[33] ZHOU Z, YI X, JIANG W, et al. Quantitative detection method for icing of horizontal-axis wind turbines[J]. Wind Energy, 2018, 22(3): 433-446.

[34] NI Z, ZHANG J, WANG M, et al. A numerical study of the anti-icing heat load for a three-dimensional aircraft wing[C]//Proceedings of the 4th International Conference on Fluid Mechanics and Industrial Applications (FMIA). [S.l.]: Journal of Physics: Conference Series, 2020: 1600012044.

[35] LIU Chunsheng, LIU Peiqing, ZHAO Yuepeng. Numberical simulation of supercooled water droplets impingement on propeller blade surfaces[J]. Chinese Journal of Computational Mechanics, 2008, 25: 95-98. (in Chinese)

[36] CAO Y, MA C, ZHANG Q, et al. Numerical simulation of ice accretions on an aircraft wing[J]. Aerospace Science and Technology, 2012, 23(1): 296-304.

[37] GUAN Ning. Numberical simulation of anti-icing thermal loads on a 3d airfoil[D]. Nanjing: Nanjing University of Aeronautics and Astronautics, 2007. (in Chinese)

[38] DUCHAINE F, BOILEAU M, SOMMERER Y, et al. Large eddy simulation of flow and heat transfer around two square cylinders in a tandem arrangement[J]. ASME Journal of Heat and Mass Transfer, 2014, 136(10): 101702.

[39] HU L Q, ZHU X C, HU C X, et al. Calculation of the water droplets local collection efficiency on the wind turbines blade[J]. Journal of Energy Resources Technology, 2017, 139(5): 051211.

[40] SHU L, LIANG J, HU Q, et al. Droplet impingement charateristics and rime ice accretion of rotating wind turbine[J]. Transactions of China Electrotechnical Society, 2016, 33(4): 800-807.

[41] CAO Y, TAN W, WU Z. Aircraft icing: An ongoing threat to aviation safety[J]. Aerospace Science and Technology, 2018, 75: 353-385.

[42] KORPRASERTSAK N, LEEPHAKPREEDA T. Real-time determination of convective heat transfer coefficient via thermoelectric modules[J]. ASME Journal of Heat and Mass Transfer, 2017, 139(10): 101701.

[43] VUKITS T. Overview and risk assessment of icing for transport category aircraft and components[C]//Proceedings of the 40th AIAA Aerospace Sciences Meeting & Exhibit. Reno: AIAA, 2002.

Acknowledgements This work was supported by the National Natural Science Foundation of China (No.12072213), the National Science and Technology Major Project from Ministry of Science and Technology of China (No.J2019-Ⅲ-0010-0054), and the National Numerical Windtunnel from China Aerodynamics Research and Center (No. NNW2019-JT01-023).

Authors Mr. **WU Zhulong** received the B.S. degree in civil engineering from Ningxia University in 2019 and M.S. degree in engineering mechanics from Sichuan University in

2022, respectively. Currently, he is a research assistant at the Basic Mechanics Laboratory of Sichuan University. His research is focused on the simulation of ice accumulation on aircraft surfaces.

Prof. **ZHOU Zhihong** received the Ph.D. degree in engineering mechanics from Northwestern Polytechnical University, Xi'an, China, in 2011. In December 2016, he joined in College of Architecture and Environment, Sichuan University. Currently, he is the Director of the Basic Mechanics Laboratory of Sichuan University. His research is focused on fundamental and engineering applications in the intersection of aircraft icing and anti-icing, low speed aerodynamics, and heat transfer.

Author contributions Mr. **WU Zhulong** calculated the data, conducted the analysis, interpreted the results, and wrote the manuscript. Prof. **YI Xian** reviewed and edited the manuscript. Mr. **XIONG Huajie** contributed to investigating the relevant literature. Prof. **ZHOU Zhihong** designed the study and provided resources. Prof. **TIAN Xiaobao** contributed to the discussion and background. All authors commented on the manuscript draft and approved the submission.

Competing interests The authors declare no competing interests.

(Production Editor: XU Chengting)

三维螺旋桨防冰热载荷分布研究

吴主龙[1], 易 贤[2], 熊华杰[1], 周志宏[1], 田晓宝[1]

(1.四川大学建筑与环境学院,成都 610065,中国; 2.中国空气动力研究与发展中心结冰与防除冰重点实验室,绵阳 621000,中国)

摘要:防冰热载荷分布预测是螺旋桨飞机防冰系统设计的关键,目前对螺旋桨飞机防冰热载荷的研究却十分匮乏。基于多参考系和Messinger热力学模型对三维螺旋桨进行了模拟,分析了防冰热载荷的影响。结果表明:防冰热载荷主要集中在叶片前缘,沿叶片展向先增大后减小;随着来流速度的增加,防冰功率及范围均先增大后减小。由于旋转效应的影响,迎角的影响可以忽略不计。此外,随着环境温度的降低,防冰功率呈线性增加。基于CCAR-25附录C规定的严重结冰条件,转速为660 r/min时,叶片的防冰范围在弦向上极限为2.1%,在弦向下极限为6.7%;防冰最大功率为9.5 kW/m^2。单台螺旋桨防冰功率超过1.96 kW。本研究为螺旋桨飞机的表面防冰提供了科学的解释,为螺旋桨飞机防冰系统的安装提供了理论依据。

关键词:飞机防冰;防冰热载荷;能量;旋转机械;螺旋桨